scientific reports

Check for updates

OPEN

Interface atom mobility and charge transfer effects on CuO and Cu_2O formation on $Cu_3Pd(111)$ and $Cu_3Pt(111)$

Yasutaka Tsuda[1,2]✉, Jessiel Siaron Gueriba[3,4], Takamasa Makino[1], Wilson Agerico Diño[3,5]✉, Akitaka Yoshigoe[2] & Michio Okada[1,6]✉

We bombarded $Cu_3Pd(111)$ and $Cu_3Pt(111)$ with a 2.3 eV hyperthermal oxygen molecular beam (HOMB) source, and characterized the corresponding (oxide) surfaces with synchrotron-radiation X-ray photoemission spectroscopy (SR-XPS). At 300 K, CuO forms on both $Cu_3Pd(111)$ and $Cu_3Pt(111)$. When we increase the surface temperature to 500 K, Cu_2O also forms on $Cu_3Pd(111)$, but not on $Cu_3Pt(111)$. For comparison, Cu_2O forms even at 300 K on Cu(111). On $Cu_3Au(111)$, Cu_2O forms only after 500 K, and no oxides can be found at 300 K. We ascribe this difference in Cu oxide formation to the mobility of the interfacial species (Cu/Pd/Pt) and charge transfer between the surface Cu oxides and subsurface species (Cu/Pd/Pt).

Metal oxides have long attracted researchers' attention, particularly the role of metal valence electrons in determining structure and properties[1,2]. Manganese (Mn) in Mn oxides, for example, can take more than one oxidation state (mixed valency). MnO_x exhibit better catalytic activity than MnO[3]. Copper (Cu) oxides also attract particular attention, due to their utility, industrial applications, abundance, low-cost, and non-toxicity. Cu_2O and CuO, two of the most common forms of Cu oxides, find applications as anodes in lithium ion battery[4] and solar cells[5]. Copper oxides are also expected to be used as catalysts for CO[6], NO dissociation[7], adsorption of H_2[8], O_2[9–11], and H_2O[12,13]. Similarly, the catalytic reactivities of Cu oxides vary with the Cu oxidation state. Several factors determine oxide formation on the surface, e.g., translational and internal (vibration and rotation) energies of impinging O_2, surface temperature, and surface electronic state[14]. Alloying allows for a simple way to vary the surface electronic state and the corresponding reactivity. For example, by alloying Cu with gold (Au) and tuning the surface composition, previous studies tried to enhance the activity and selectivity of Cu–Au nanoparticle catalysts for CO_2 reduction[15,16]. On $Cu_3Au(111)$, the presence of (the "inert") Au hinders O_2 dissociative adsorption, as compared to Cu(111)[17–20]. At surface temperature $T_S = 300$ K, Au-rich layers, formed between the bulk and surface, prevents Cu oxide formation further into bulk. Atom diffusion at $T_S = 500$ K promotes Cu_2O formation, but leaves a protective Au-rich layer that prevents further oxidation into the bulk. On the other hand, Cu–palladium (Pd) alloys synergetically enhanced CO_2 hydrogenation to alcohol, as compared to mono-metallic catalysts[21,22]. Cu–platinum (Pt) alloys, viz., $Pt_{34.5}Cu_{65.5}$, also showed superior methanol oxidation and oxygen reduction performance[23]. Moreover, single Pt atoms at the Cu metal-oxide interface promote the reduction of Cu_2O by H_2 exposure[24]. These results indicate that choosing the right alloy components strongly affect reactivity. Here, we report on how alloying Cu with Pd and Pt, elements known to be more reactive than Au, affects oxidation of the corresponding surfaces. We bombarded $Cu_3Pd(111)$ and $Cu_3Pt(111)$ with a 2.3 eV hyperthermal oxygen molecular beam (HOMB) source, and characterized the corresponding (oxidized) surfaces using X-ray photoemission spectroscopy (XPS) in conjunction with synchrotron radiation (SR). We found that the presence of interfacial Pd and Pt, between surface Cu oxides and bulk, suppresses atomic diffusion and induces charge transfer near the interface. These result in the formation of protective layers that prevent Cu oxidation further

[1]Department of Chemistry, Osaka University, Toyonaka, Osaka 560-0043, Japan. [2]Materials Sciences Research Center, Japan Atomic Energy Agency, 1-1-1 Kouto, Sayo-cho, Sayo-gun, Hyogo 679-5148, Japan. [3]Department of Applied Physics, Osaka University, Suita, Osaka 565-0871, Japan. [4]Department of Physics, De La Salle University, 2401 Taft Avenue, Manila 0922, Philippines. [5]Center for Atomic and Molecular Technologies, Osaka University, Suita, Osaka 565-0871, Japan. [6]Institute for Radiation Sciences, Osaka University, Toyonaka, Osaka 560-0043, Japan. ✉email: tsuda.yasutaka@jaea.go.jp; wilson@dyn.ap.eng.osaka-u.ac.jp; okada@chem.sci.osaka-u.ac.jp

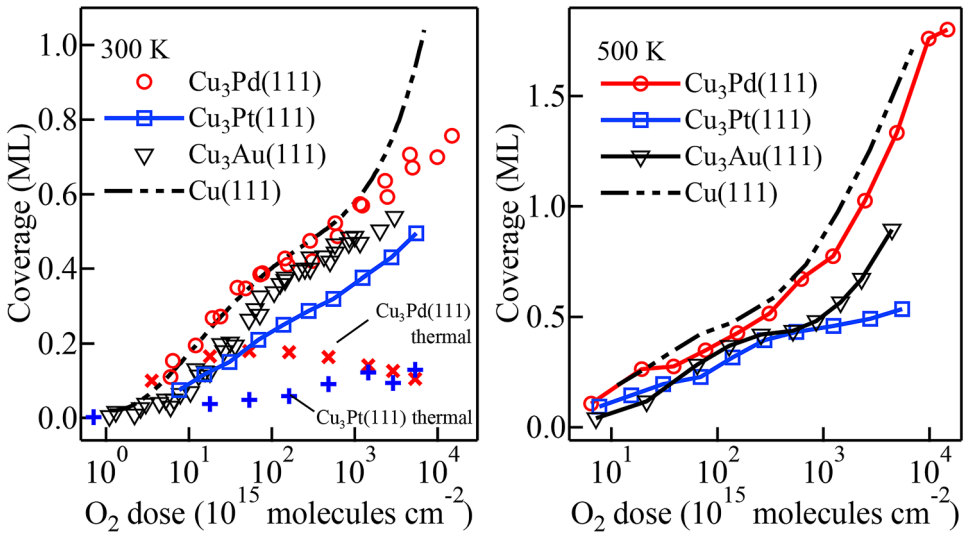

Figure 1. O uptake curves for $Cu_3Pd(111)$ and $Cu_3Pt(111)$ after 2.3 eV HOMB irradiation at $T_S = 300$ and 500 K. For reference, O uptake curves taken after thermal O_2 exposure, and O uptake curves for Cu(111) and $Cu_3Au(111)$ after 2.3 eV HOMB irradiation, are also shown.

Sample		1st layer	2nd layer	3rd layer	4th layer
		x_1	x_2	x_3	x_4
$Cu_3Pd(111)$	Experiment[a]	44	22	Bulk(25)	Bulk(25)
	Theory[a]	50	25	Bulk(25)	Bulk(25)
$Cu_3Pt(111)$	Experiment[a]	23	33	88	20
	Experiment[25]	20	31	Bulk(25)	Bulk(25)
	Experiment[26]	28	8	48	8
	Theory[a]	100	0	50	Bulk(25)

Table 1. Layer concentration profiles x_n (in units of %-Pd or %-Pt) for clean $Cu_3Pd(111)$ and $Cu_3Pt(111)$. [a]This work.

into the bulk. These also account for the difference in Cu valencies and resulting oxidation states (Cu oxide species formed) on $Cu_3Pd(111)$ and $Cu_3Pt(111)$, as compared to Cu(111) and $Cu_3Au(111)$.

Results

Pd and Pt (surface) concentration profiles. In Table 1, we show the corresponding experimental and calculated layer concentration profiles x_n (in units of %-Pd or %-Pt) for clean $Cu_3Pd(111)$ and $Cu_3Pt(111)$. To experimentally determine the corresponding Pd and Pt layer concentrations x_n, of the nth layer from the vacuum, we followed the method described in previous studies[17], using the photoelectron detection angle dependence of the intensities of the bulk (B-) and surface (S-) components of the Pd-3*d* and Pt-4*f* XPS spectra. (For more details on the procedures, analyses, and calculations, cf., Section S.1 in the supplementary information.)

On the $Cu_3Pd(111)$, our experimental analyses (calculation results) show a Pd concentration of x_1= 44 (50) (cf., first two rows, Table 1), which is greater than the bulk value of $x_{bulk} = 25$. This indicates Pd segregation onto the surface, resulting in a Pd-rich surface.

On the $Cu_3Pt(111)$, our experimental analyses show $x_1 = 23$, $x_2 = 33$, and $x_3 = 88$ (cf., third row, Table 1). This indicates Pt segregation onto the 2nd and 3rd layers (Pt-rich 2nd and 3rd layers). Previous studies using low energy ion scattering (LEIS) [25] report similar results, viz., $x_1 = 20$, $x_2 = 31$ (cf., fourth row, Table 1). For comparison, low energy electron diffraction (LEED) studies[26] report $x_1 = 28$, $x_2 = 8$, $x_3 = 48$, and $x_4 = 8$ (cf., fifth row, Table 1). On the other hand, calculation results show 100%-Pt segregation onto the 1st (surface) layer, and 50% Pt segregation onto the 3rd layer. Regardless, both experiment and theory show (on the average) similar Pt concentrations from the 1st to the 3rd layer, viz., 48% and 50%, respectively.

LEED patterns. The clean $Cu_3Pd(111)$ exhibits a (2×2) LEED pattern with some spot splittings (cf., Fig. S.4(a) in the supplementary information), which we ascribe to the presence of structural anti-phase domains on the surface (considering the 44%-Pd surface segregation and three rotationally symmetric domains). For comparison, the clean $Cu_3Pt(111)$ exhibits a (1×1) LEED pattern, indicating random distribution of 23%-Pt atoms on the 1st layer.

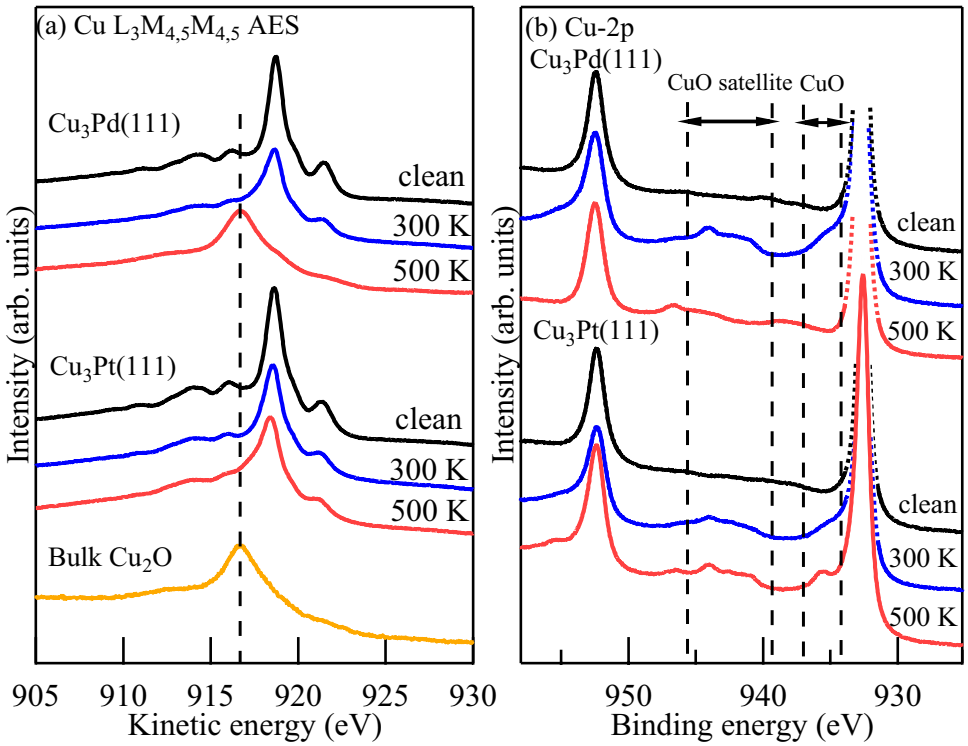

Figure 2. (**a**) Cu-$L_3M_{4,5}M_{4,5}$ AES and (**b**) Cu-2*p* XPS spectra of $Cu_3Pd(111)$ and $Cu_3Pt(111)$, taken after 2.3 eV HOMB irradiation at $T_S = 300$ K and 500 K, at a photoelectron detection angle $\theta = 70°$ from the surface normal. For $Cu_3Pd(111)$, corresponding AES spectra for O-coverages of 0 ML (clean), 0.76 ML at 300 K, and 1.8 ML at 500 K, are shown. Similarly, for $Cu_3Pt(111)$, corresponding AES spectra for O-coverages of 0 ML (clean), 0.49 ML at 300 K, 0.53 ML at 500 K, are shown. Bulk Cu_2O spectra also shown in (**a**) for reference, with dashed vertical line indicating characteristic Cu_2O peak position.

	$Cu_3Pd(111)$	$Cu_3Pt(111)$	$Cu(111)$[14,15]	$Cu_3Au(111)$[17–20]
300 K	CuO	CuO	Cu_2O	Only chemisorbed O
500 K	Cu_2O	CuO	Cu_2O	Cu_2O

Table 2. Oxides species formed on Cu and Cu-based alloys after 2.3 eV HOMB irradiation at $T_S = 300$ K.

Oxygen uptake curves. In Fig. 1, we show the O uptake curves for $Cu_3Pd(111)$ and $Cu_3Pt(111)$ produced by integrating a series of O-1*s* XPS spectra measured after 2.3 eV HOMB irradiation at $T_S = 300$ and 500 K (also cf., Fig. S.6 in supplementary information). We determined the oxygen coverage by comparing Cu(100)-$(2\sqrt{2} \times \sqrt{2})$-O and Cu(110)-$(2 \times 1)$-O[27] and also cross-checked by using the intensity ratios of O-1*s*/Pd-3*d* and O-1*s*/Pt-4*f*. For comparison, we also show the O uptake curves taken after thermal O_2 exposure, and the O uptake curves for Cu(111) and $Cu_3Au(111)$ taken after 2.3 eV HOMB irradiation. Comparing the results of HOMB irradiation and thermal O_2 exposure, we confirm the need for higher translational energies to realize effective oxide formation. However, following procedures previously reported for determining Au concentrations on the oxidized $Cu_3Au(111)$[17], we were not able to consistently obtain the Pd and Pt concentrations. This may be due to the presence of Cu oxide islands on the corresponding surfaces, whereas only homogeneous adsorbed-O forms on $Cu_3Au(111)$[17,28].

Cu-$L_3M_{4,5}M_{4,5}$ and Cu-2*p* spectra. In Fig. 2, we show the Cu-$L_3M_{4,5}M_{4,5}$ AES (Auger electron spectroscopy) and Cu-2*p* XPS spectra of the corresponding Cu oxides formed on $Cu_3Pd(111)$ and $Cu_3Pt(111)$. For reference, note the Cu_2O features appearing at ca. 917 eV kinetic energy (cf., bulk Cu_2O peak, Fig. 2a). From Fig. 2a, we find prominent Cu_2O formation only for $Cu_3Pd(111)$ oxidized at $T_S = 500$ K. On the other hand, in Fig. 2b, we find characteristics of CuO (cf., shoulder at ca. 936 eV and satellite peaks between ca. 939 eV and 946 eV[29]) for both $Cu_3Pd(111)$ and $Cu_3Pt(111)$ oxidized at $T_S = 300$ K. We also see that these CuO features persist at $T_S = 500$ K for $Cu_3Pt(111)$, but disappear for $Cu_3Pd(111)$. On $Cu_3Pt(111)$, AES spectra analyses indicate CuO formation only, both at $T_S = 300$ K and 500 K. On $Cu_3Pd(111)$, AES spectra analyses indicate CuO formation at $T_S = 300$ K and Cu_2O formation at $T_S = 500$ K. (Pd-3*d* and Pt-4*f* XPS spectra analyses also indicate that only

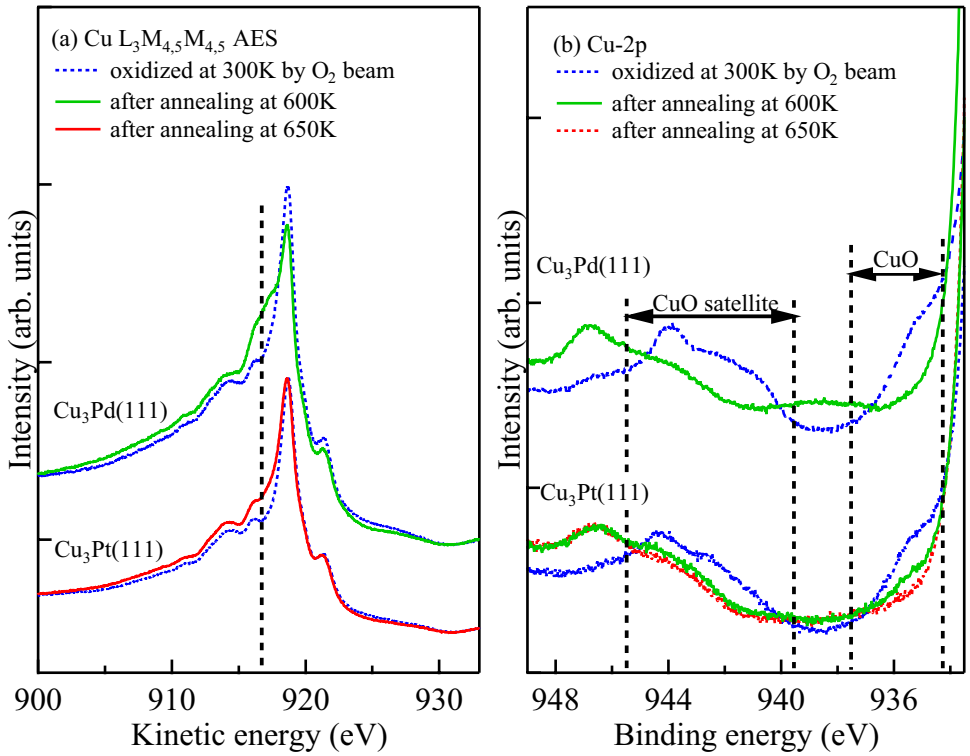

Figure 3. (**a**) Cu-$L_3M_{4,5}M_{4,5}$ AES and (**b**) Cu-2*p* spectra of $Cu_3Pd(111)$ and $Cu_3Pt(111)$, taken after 2.3 eV HOMB irradiation at $T_S = 300$ K, and after annealing at 600 K and 650 K, at a photoelectron detection angle of 70° from the surface normal. $Cu_3Pd(111)$ has 0.50 ML CuO-coverage and $Cu_3Pt(111)$ has ca. 0.50 ML CuO-coverage, before annealing. Characteristic Cu_2O peak position indicated as dashed vertical line in (**a**), for reference.

Cu oxidation occurs on both $Cu_3Pd(111)$ and $Cu_3Pt(111)$, cf., Section S.4 in supplementary information). In Table 2, we show a summary of oxides formed on the Cu and Cu-based alloy surfaces studied.

In Fig. 3, we show the effect of annealing on the corresponding Cu-$L_3M_{4,5}M_{4,5}$ AES and Cu-2*p* spectra of $Cu_3Pd(111)$ and $Cu_3Pt(111)$ oxidized at $T_S = 300$ K. We see enhanced Cu_2O features from the Cu-$L_3M_{4,5}M_{4,5}$ spectra, and diminished CuO features from the Cu-2*p*. (The fitted O-1*s* XPS spectra also show enhanced Cu_2O features and diminished CuO features, cf., Fig. S.9 in supplementary information). This suggests the reduction of CuO into Cu_2O at high T_S. However, a lingering CuO peak remains on $Cu_3Pt(111)$, even after the annealing at $T_S = 600$ K, which we no longer see on $Cu_3Pd(111)$. We found that annealing at $T_S = 650$ K completes the reduction from CuO to Cu_2O on the $Cu_3Pt(111)$. Therefore, we conclude more stable CuO formation on $Cu_3Pt(111)$ as compared to $Cu_3Pd(111)$. Similar effect can be observed for Cu(410) oxidation at lower T_S. After 2.2 eV HOMB irradiation, CuO forms on Cu(410) at $T_S = 100$ K[30]. Annealing at $T_S = 273$ K reduces CuO into Cu_2O. Alloying increases the corresponding transition temperature from CuO to Cu_2O. CuO persists even at $T_S = 300$ K.

Discussions

O_2 Dissociation, CuO and Cu_2O formation on Cu and Cu alloys in the early stage of oxidation. The position of the surface *d*-band center relative to the Fermi level[31,32] has often been used to qualitatively discuss reactivity of dissociative adsorption. The deeper the surface *d*-band center, the less reactive the surface. From XPS measurements, in order of increasing depth with respect to the vacuum level (viz., in order of decreasing reactivity), we have Cu_3Pd (−2.7 eV), Cu_3Pt (−2.9 eV), Cu (−3.1 eV), and finally Cu_3Au (−3.7 eV) (also cf., Fig. S.10 in supplementary information, and Ref.[33]). However, the uptake curves in Fig. 1 show different tendency of reactivity. We see O-coverages lower than what we would expect from the *d*-band for both $Cu_3Pd(111)$ and $Cu_3Pt(111)$.

Now, let us consider what the uptake curves taken at $T_S = 300$ K and 500 K tell us (cf., Fig. 1). Here, we discuss the early stage of oxidation where only the dissociative adsorption of O_2 occurs on Cu(111). Note that on Cu(111) and $Cu_3Au(111)$, previous HOMB irradiation studies at 2.3 eV[34] report that direct O_2 dissociative adsorption dominates at the early stage of oxidation, and Cu oxide (Cu_2O) subsequently forms above $\sim 10^{17}$ molecules cm^{-2}. In comparison, $Cu_3Pd(111)$ and $Cu_3Pt(111)$ show Cu oxide (CuO) formation above ca. 8–60 $\times 10^{15}$ molecules cm^{-2} as shown in Fig. S.8 in supplementary information. In other words, Cu oxide forms earlier on $Cu_3Pd(111)$ and $Cu_3Pt(111)$ than on Cu(111). Taking this into account, we can interpret the reactivity below $\sim 10^{17}$ molecules cm^{-2} as follows. The inactive CuO formed at an early stage of oxidation makes $Cu_3Pd(111)$ and $Cu_3Pt(111)$ more robust to further oxidation of bulk Cu, while further bulk Cu is lost

through Cu_2O formation on Cu(111). The earlier CuO formation at ca. 8×10^{15} molecules cm^{-2} further indicates a more robust $Cu_3Pt(111)$ than $Cu_3Pd(111)$. So, based on the corresponding O uptake curves, we have Cu(111), $Cu_3Pd(111)$, $Cu_3Au(111)$[20], and $Cu_3Pt(111)$, in order of decreasing susceptibility to Cu loss (i.e., Cu_2O formation).

The protective layer. The difference in efficiency of oxide formation between Cu and Cu alloy surfaces can be ascribed to the resulting protective layer of Pd (Pt) layer formed at the interface between the bulk and surface Cu oxide (cf., e.g., $Cu_3Au(111)$[20]). As mentioned in S.4 in supplementary information, only Cu oxidation occurs on $Cu_3Pd(111)$ and $Cu_3Pt(111)$. Previous studies also show that only Cu oxide forms on Cu-Pt alloy[28] and Cu deposited on Pt(111)[35]. The selective Cu oxidation results in Pd- and Pt-rich interface layers. We see a steep O uptake curve, coming from Cu_2O formation[34], for Cu(111) at $T_S = 300$ K (cf., Fig. 1 (left-panel), region above ca. 10^{17} molecules cm^{-2}). On Cu(111), Cu_2O formation occurs due to collision induced absorption (CIA)[36]. On Cu_3Au, the inert Au interface layer prevents O atoms from diffusing further into the bulk by CIA process. As a result, Cu oxide hardly forms at 300 K[17–20]. Here, we find that the interface Pd- and Pt- layers also prevent O diffusion further into the bulk to realize the CIA process. It also prevents Cu diffusion from the bulk to the surface CuO.

Mobility/diffusion. At $T_S = 500$ K, we expect that the increased temperature would enhance atom diffusion, allowing for Cu oxide formation further into the bulk. On $Cu_3Au(111)$, Cu_2O forms at 500 K[19]. $Cu_3Pd(111)$ also has a steeper O uptake curve at 500 K than at 300 K (cf., above 10^{17} molecules cm^{-2} in Fig. 1). However, $Cu_3Pt(111)$ remains relatively inactive, even at 500 K. This is because of the presence of less mobile Pt at the interface. In Cu, Pd has an activation/diffusion barriers of ca. 0.88 eV[37], Au has 1.1 eV[38], and Pt has 1.51 eV[39]. This is consistent with the reactivity observed above ca. 10^{17} molecules cm^{-2} at 500 K, i.e., the region where mainly CuO forms. The interface Pt suppresses Cu oxide growth into the bulk even at 723 K[28]. Cu diffusion through the Pd (Pt) interface would also be unlikely considering the high Cu diffusion barriers (ca. 2.5 eV in Pd, 2.75 eV in Pt, and 2.0 eV in Au)[40]. As expected, these differences in diffusion barriers affect the kind of Cu oxides formed on the Cu alloy surfaces.

At 100 K, metastable CuO forms on Cu(410)[30]. The low temperature suppresses O diffusion from the surface to the bulk (and also Cu diffusion from the bulk to the surface), while collision induced absorption (CIA) allows for a continuous supply of O atoms to the surface. We can expect similar effects on the Cu-Pd and Cu-Pt alloy surfaces.

At 300 K, the presence of Pd or Pt at the corresponding interfaces suppresses the diffusion of O and Cu, while CIA allows for a continuous supply of O atoms on the surface. Similarly, on $Cu_3Au(111)$ at 300 K, O atoms adsorbed on surface cannot diffuse into bulk due to the interface Au[17,18]. As a result, no Cu oxides form on $Cu_3Au(111)$ at 300 K.

At 500 K, enhanced diffusion allows oxidation further into the bulk of $Cu_3Au(111)$ and $Cu_3Pd(111)$, and we find growth of the thermodynamically more stable Cu_2O. On the other hand, CuO persists on Cu_3Pt at 500 K because of the higher Pt diffusion barrier. As shown in Fig. 3, Cu_2O forms after annealing (after the HOMB irradiation at 300 K). Higher T_S enables O diffusion further into the bulk and further Cu supply to the surface CuO. This occurs at $T_S = 650$ K on Cu_3Pt, and $T_S = 600$ K on Cu_3Pd. The less diffusive Pt present at the interface prevents further Cu_2O formation as compared to Pd. At $T_S = 723$ K, Cu_2O islands grow on Cu-Pt alloy. However, the oxide does not grow deeper into bulk even at high temperature because of less diffusivity of Pt[28].

Charge distribution. In Fig. 4, for 0.5 ML-O adsorbed on $Cu_3Pt(111)$, we see that in the early stage of oxidation, Cu segregates to the surface and oxidized to form CuO. The charge distribution also shows that the more electronegative Pt competes with O for the Cu electrons. This, together with the mobility arguments presented earlier, accounts for why Cu_2O easily forms on Cu(111) and not on Cu-alloys. Note that this could also consistently explain previous reports for that electron transfer from the metal substrate (Au, Ni, Mo, Cu, V) to the metal oxide resulted in Mo^{6+} reduction to Mo^{4+} and/or Mo^{5+} near the interface[41]. Conversely, in our case, electron transfer results in Cu^{+} oxidation to Cu^{2+} as shown in Fig. S.11 in supplementary information. Additionally, the presence of single Pt atoms at the Cu metal-oxide interface weakens Cu-O bond[24], consistent with the preferential formation of CuO (Cu–O: 0.188 and 0.196 nm) than Cu_2O (Cu–O: 0.185 nm) on Pt interface[42].

Summary and conclusions

In conclusion, we studied the oxidation of $Cu_3Pd(111)$ and $Cu_3Pt(111)$, using 2.3 eV hyperthermal oxygen molecular beam (HOMB) source, and synchrotron-radiation X-ray photoemission spectroscopy (SR-XPS) for surface characterization. We determined the Pd- and Pt- layer profiles of $Cu_3Pd(111)$ and $Cu_3Pt(111)$ from the corresponding Pd-3*d* and Pt-4*f* spectra. At 300 K, we found mainly (only) the presence of CuO on both $Cu_3Pd(111)$ and $Cu_3Pt(111)$. At 500 K, we found Cu_2O on $Cu_3Pd(111)$, and only CuO on $Cu_3Pt(111)$. For comparison, at 300 K, Cu_2O forms on Cu(111), and no oxides form on $Cu_3Au(111)$. The early formation of Cu oxides on $Cu_3Pd(111)$ and $Cu_3Pt(111)$ results in hindered reactivity (susceptibility) to further oxidation into the bulk (resulting in the formation of Cu_2O) as compared to Cu. Cu oxide formation depends on the Cu alloy component and temperature. We ascribe this difference/preference of Cu oxide species to the mobility of the interfacial Cu/Pd/Pt, and the charge transfer between the initial (pre-oxidized) surface (Cu) and subsurface (Cu, Pd, or Pt) species. The presence of Cu_2O and metastable CuO at the Pd and Pt interface could play an important role in catalytic reactions. We showed that we can control the oxidation state of the surface metal oxide by alloying, which in turn would allow us to control the catalytic reactivity of the oxides.

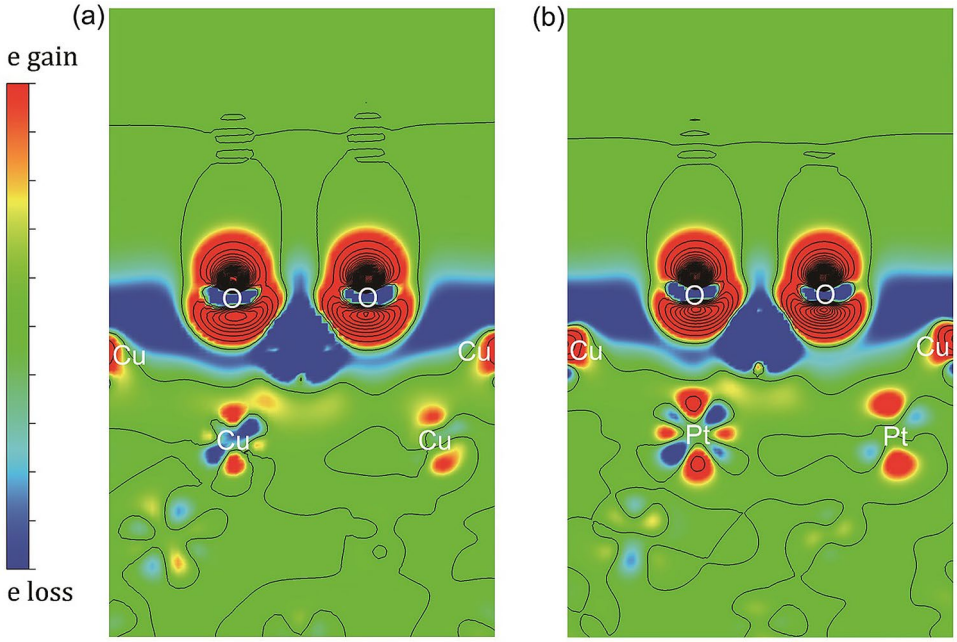

Figure 4. Calculated charge distribution difference for 0.5 ML-O adsorbed on $Cu_3Pt(111)$, for layer concentrations (**a**) $(x_1, x_2, x_{3-7}) = (0, 0, 25)$ and (**b**) $(x_1, x_2, x_{3-7}) = (0, 100, 25)$. We obtained (**a**) and (**b**) by subtracting the charge distributions of bulk slab and O atoms from that of O-adsorbed slab. We can see a relatively higher electron gain around Pt in the second layer (**b**) than that around Cu (**a**). The electronegative O atoms are relatively far from the Pt subsurface layer. Thus, we associate the charge gain of Pt with the charge loss of surface Cu atoms.

Method

Experiments. We performed all experiments with the surface reaction analysis apparatus (SUREAC 2000) built at BL23SU in SPring-8[17–20,43,44], with the base pressure of $< 2 \times 10^{-8}$ Pa. Briefly, our surface reaction analysis chamber has an electron energy analyzer (OMICRON EA125-5MCD) and a Mg/Al-Kα twin-anode x-ray source (OMICRON DAR400). We also have a quadrupole mass spectrometer, for monitoring the molecular beam, located opposite to the HOMB (hyperthermal oxygen molecular beam) source. We purchased $Cu_3Pd(111)$ and $Cu_3Pt(111)$ samples from SPL and MaTeck, respectively. We cleaned the $Cu_3Pd(111)$ and $Cu_3Pt(111)$ samples by repeated sputtering with Ar^+ and annealing for 20 min ($Cu_3Pd(111)$: 1.0 keV, 723 K, $Cu_3Pt(111)$: 0.5 keV, 773 K), until the impurities were no longer detectable by SR-XPS (synchrotron-radiation X-ray photoemission spectroscopy). We generated a HOMB by the free expansion of mixed gas of O_2, He and/or Ar from a nozzle with a small orifice. The translational energy of HOMB, E_{SG} can be expressed as:

$$E_{SG} = S^2 \cdot R \cdot T_0 \cdot \frac{m_{SG}}{m_s}, \tag{1}$$

where S (= 1.557) is a factor that is expressed by using the Mach number, R (= 8.617×10^{-5} eV $\cdot$ K^{-1}) is gas constant, T_0 is the nozzle temperature, m_{SG} is the mass of the reactant gas (O_2) and m_s is the reduced mass of the mixed gas (He and/or Ar). By changing the gas mixing ratios at the nozzle and nozzle temperature T_0, we can control the kinetic energy of the incident HOMB, E_{SG}. The detailed explanation for HOMB generation is shown in Refs.[45,46]. We set the nozzle temperature to 1400 K, obtaining a 2.3 eV HOMB. We irradiate the sample surface with a HOMB (along the surface normal) at $T_S = 300$ and 500 K. The pressure during the HOMB irradiation is about 1×10^{-5} Pa. The oxidation by the scattered O_2 which causes the pressure increase is not important because the percentage of O_2 in the gas is only 1% for the 2.3 eV HOMB, and the oxidation by thermal O_2 is less reactive than by HOMB as shown in Fig. 1. After each irradiation, we then obtained the corresponding high-resolution SR-XPS spectra at $T_S = 300$ K, at detection angles of $\theta = 0^\circ$ and 70° from the surface normal, using a monochromatic SR beam with a photon energy of 1100 eV. We performed the HOMB irradiations at $T_S = 300$ and 500 K.

Theoretical calculations. We performed density functional theory (DFT)-based total energy calculations as implemented in the Vienna Ab Initio Simulation Package[47,48], within the generalized gradient approximation (GGA)[49], using plane waves (600 eV cutoff energy) and the projector augmented wave method[50]. To model $Cu_3Pd(111)$ and $Cu_3Pt(111)$, we used slabs. Each slab has seven fcc(111) layers, separated by ca. 1.50 nm (Cu_3Pd) and 0.7 nm (Cu_3Pt) vacuum, repeated in a supercell geometry (shown in Fig. S.2). We also applied dipole corrections. Each layer in the slab contains 4 atoms, so that the composition (of Pd or Pt) can be varied in steps of 25%. Convergence tests for k-point meshes and cutoff energy values were performed (cf., Table. S.1). We have chosen sufficiently large supercells so as to avoid interaction between adsorbates in the neighboring super-

cells. We performed Brillouin zone integration using the Monkhorst-Pack special *k*-point sampling technique[51], with $8 \times 8 \times 1$ (Cu_3Pd) and $6 \times 6 \times 1$ (Cu_3Pt) sampling meshes. We kept the bottom five (four) layers of Cu_3Pd (Cu_3Pt), which comprise the unsegregated layers having bulk stoichiometry, viz., 25%-Pd (or Pt) 75%-Cu in the $L1_2$ ordered structure, fixed to the optimized theoretical bulk lattice constant 0.3723 nm (0.3730 nm). We allowed the top three layers, which constitute the segregated layers, viz., the first surface layer, the second-, and third-(sub-surface) layers, to relax. In addition to calculations for the slab, we also carried out similar calculations for bulk Cu, bulk Pd, bulk Pt, bulk Cu_3Pd and bulk Cu_3Pt.

Data availavility

All data needed to evaluate the conclusions in the paper are present in the paper and/or the Supplementary Information. Additional data related to this paper may be requested from the authors.

Received: 21 October 2020; Accepted: 18 January 2021
Published online: 15 February 2021

References

1. Rao, C. N. R. Transition metal oxides. *Annu. Rev. Phys. Chem.* **40**, 291–326 (1989).
2. Chavali, M. S. & Nikolova, M. P. Metal oxide nanoparticles and their applications in nanotechnology. *SN Appl. Sci.* **1**, 607 (2019).
3. Indra, A. *et al.* Active mixed-valent MnO_x water oxidation catalysts through partial oxidation (corrosion) of nanostructured MnO particles. *Angew. Chem. Int. Ed.* **52**, 13206–13210 (2013).
4. Park, J. C., Kim, J., Kwon, H. & Song, H. Gram-scale synthesis of Cu_2O nanocubes and subsequent oxidation to CuO hollow nanostructures for lithium-ion battery anode materials. *Adv. Mater.* **21**, 803–807 (2009).
5. Wong, T. K. S., Zhuk, S., Masudy-Panah, S. & Dalapati, G. K. Current status and future prospects of copper oxide heterojunction solar cells. *Materials* **9**, 271 (2016).
6. Zedan, A. F., Mohamed, A. T., El-Shall, M. S., AlQaradawi, S. Y. & AlJaber, A. S. Tailoring the reducibility and catalytic activity of CuO nanoparticles for low temperature CO oxidation. *RSC Adv.* **8**, 19499–19511 (2018).
7. Kishi, H. *et al.* A theoretical study of the reactivity of $Cu_2O(111)$ surfaces: the case of NO dissociation. *J. Phys. Condens. Matter* **24**, 262001 (2012).
8. Yu, X., Zhang, X., Wang, H., Wang, Z. & Feng, G. High-coverage H_2 adsorption on the reconstructed $Cu_2O(111)$ surface. *J. Phys. Chem. C* **121**, 22081–22091 (2017).
9. Yu, X., Zhang, X., Tian, X., Wang, S. & Feng, G. Density functional theory calculations on oxygen adsorption on the Cu_2O surfaces. *Appl. Surf. Sci.* **324**, 53–60 (2015).
10. Yu, X., Zhang, X., Wang, S. & Feng, G. A first principle study on the magnetic properties of Cu_2O surfaces. *Curr. Appl. Phys.* **15**, 1303–1311 (2015).
11. Yu, X., Zhao, C., Zhang, T. & Liu, Z. Molecular and dissociative O_2 adsorption on the $Cu_2O(111)$ surface. *Phys. Chem. Chem. Phys.* **20**, 20352–20362 (2018).
12. Yu, X., Zhang, X., Wang, S. & Feng, G. A computational study on water adsorption on $Cu_2O(111)$ surfaces: The effects of coverage and oxygen defect. *Appl. Surf. Sci.* **343**, 33–40 (2015).
13. Yu, X. & Zhang, X. High coverage water adsorption on CuO(011) surface. *Phys. Chem. Chem. Phys.* **19**, 18652–18659 (2017).
14. Montemore, M. M., van Spronsen, M. A., Madix, R. J. & Friend, C. M. O_2 activation by metal surfaces: implications for bonding and reactivity on heterogeneous catalysts. *Chem. Rev.* **118**, 2816–2862 (2017).
15. Kim, D., Resasco, J., Yu, Y., Asiri, A. M. & Yang, P. Synergistic geometric and electronic effects for electrochemical reduction of carbon dioxide using gold-copper bimetallic nanoparticles. *Nat. Commun.* **5**, 1–8 (2014).
16. Liu, K. *et al.* Electronic effects determine the selectivity of planar Au–Cu bimetallic thin films for electrochemical CO_2 reduction. *ACS Appl. Mater. Interfaces* **11**, 16546–16555 (2019).
17. Tsuda, Y. *et al.* Initial stages of $Cu_3Au(111)$ oxidation: oxygen induced Cu segregation and the protective Au layer profile. *Phys. Chem. Chem. Phys.* **16**, 3815–3822 (2014).
18. Oka, K. *et al.* The effects of alloying and segregation for the reactivity and diffusion of oxygen on $Cu_3Au(111)$. *Phys. Chem. Chem. Phys.* **16**, 19702–19711 (2014).
19. Tsuda, Y., Yoshigoe, A., Teraoka, Y. & Okada, M. Surface temperature dependence of oxidation of $Cu_3Au(111)$ by an energetic oxygen molecule. *Mater. Res. Express* **3**, 035014 (2016).
20. Okada, M. *et al.* Experimental and theoretical studies on oxidation of Cu–Au alloy surfaces: effect of bulk Au concentration. *Sci. Rep.* **6**, 31101 (2016).
21. Jiang, X., Koizumi, N., Guo, X. & Song, C. Bimetallic Pd–Cu catalysts for selective CO_2 hydrogenation to methanol. *Appl. Catal. B Environ.* **170**, 173–185 (2015).
22. Bai, S. *et al.* Highly active and selective hydrogenation of CO_2 to ethanol by ordered Pd-Cu nanoparticles. *J. Am. Chem. Soc.* **139**, 6827–6830 (2017).
23. Li, C. *et al.* Composition-driven shape evolution to Cu-rich PtCu octahedral alloy nanocrystals as superior bifunctional catalysts for methanol oxidation and oxygen reduction reaction. *Nanoscale* **10**, 4670–4674 (2018).
24. Schilling, A. C. *et al.* Accelerated Cu_2O reduction by single pt atoms at the metal-oxide interface. *ACS Catal.* **10**, 4215–4226 (2020).
25. Shen, Y. G., O'Connor, D. J., Wandelt, K. & MacDonald, R. J. Studies of surface composition and structure of $Cu_3Pt(111)$ by low energy alkali ion scattering. *Surf. Sci.* **328**, 21–31 (1995).
26. Gauthier, Y. *et al.* An unusual composition profile: a LEED-TBIM study of $Pt_{25}Cu_{75}(111)$. *Surf. Sci.* **527**, 71–79 (2003).
27. Okada, M. *et al.* Actively controlled oxidation of Cu{100} with hyperthermal O_2 molecular beam. *J. Chem. Phys.* **119**, 6994–6997 (2003).
28. Luo, L. *et al.* Comparative study of the alloying effect on the initial oxidation of Cu–Au(100) and Cu–Pt(100). *Appl. Phys. Lett.* **104**, 121601 (2014).
29. Ghijsen, J. *et al.* Electronic structure of Cu_2O and CuO. *Phys. Rev. B* **38**, 11322–11330 (1988).
30. Okada, M. *et al.* X-ray photoemission study of the temperature-dependent CuO formation on Cu(410) using an energetic O_2 molecular beam. *Phys. Rev. B* **75**, 233413 (2007).
31. Goto, K. *et al.* (eds) *Exercises in Quantum Mechanics-Detailed Explanation, Theory and Application 376–377* (Kyoritsu Publishing, Bunkyo-ku, 1982).
32. Hammer, B. & Norskov, J. K. Why gold is the noblest of all the metals. *Nature* **376**, 238–240 (1995).
33. Ruban, A., Hammer, B., Stoltze, P., Skriver, H. L. & Nørskov, J. K. Surface electronic structure and reactivity of transition and noble metals. *J. Mol. Catal. A Chem.* **115**, 421–429 (1997).
34. Moritani, K. *et al.* Photoemission study of the translational energy induced oxidation processes on Cu(111). *J. Vac. Sci. Technol. A Vacuum Surfaces Films* **22**, 1625–1630 (2004).
35. Gloystein, A. & Nilius, N. Copper oxidation on Pt(111)- More than a surface oxide?. *J. Phys. Chem. C* **123**, 26939–26946 (2019).

36. Okada, M. *et al.* Actively controlled oxidation of Cu{100} with hyperthermal O_2 molecular beam. *J. Chem. Phys.* **119**, 6994–6997 (2003).
37. Grant, M. L., Swartzentruber, B. S., Bartelt, N. C. & Hannon, J. B. Diffusion kinetics in the Pd/Cu(001) surface alloy. *Phys. Rev. Lett.* **86**, 4588–4591 (2001).
38. Aleshin, A. N., Bokstein, B. S., Egorov, V. K. & Kurkin, P. V. Grain boundary and bulk diffusion in Au-Cu thin films. In *Defect and Diffus. Forum*, vol. 95, 457–462 (Trans Tech Publ, 1993).
39. Aleshin, A. N., Egorov, V. K., Bokstein, B. S. & Kurkin, P. V. Study of Pt diffusion in thin copper films under two kinetic regimes. *J. Appl. Phys.* **77**, 6239–6243 (1995).
40. Wu, H., Mayeshiba, T. & Morgan, D. High-throughput ab-initio dilute solute diffusion database. *Sci. Data* **3**, 1–11 (2016).
41. Greiner, M. T., Chai, L., Helander, M. G., Tang, W.-M. & Lu, Z.-H. Metal/metal-oxide interfaces: how metal contacts affect the work function and band structure of MO_3. *Adv. Funct. Mater.* **23**, 215–226 (2013).
42. Ching, W. Y., Xu, Y.-N. & Wong, K. W. Ground-state and optical properties of Cu_2O and CuO crystals. *Phys. Rev. B* **40**, 7684–7695 (1989).
43. Okada, M. *et al.* Protective layer formation during oxidation of $Cu_3Au(111)$ using hyperthermal O_2 molecular beam. *Appl. Phys. Lett.* **89**, 201912 (2006).
44. Okada, M. *et al.* Comparative study of oxidation on Cu and Cu_3Au surfaces with a hyperthermal O_2 molecular beam. *Surf. Sci.* **600**, 4228–4232 (2006).
45. Okada, M. & Teraoka, Y. Molecular-Beam Controlled Chemical Reactions on Si Surfaces. In *Encyclopedia of Semiconductor Nanotechnology* Vol. 4 (ed. Umar, A.) 61–111 (American Scientific Publishers, Los Angeles, 2017).
46. Ogawa, S. *et al.* Gas barrier properties of chemical vapor-deposited graphene to oxygen imparted with sub-electronvolt kinetic energy. *J. Phys. Chem. Lett.* **11**, 9159–9164 (2020).
47. Kresse, G. & Furthmüller, J. Efficiency of ab-initio total energy calculations for metals and semiconductors using a plane-wave basis set. *Comput. Mater. Sci.* **6**, 15–50 (1996).
48. Kresse, G. & Furthmüller, J. Efficient iterative schemes for ab initio total-energy calculations using a plane-wave basis set. *Phys. Rev. B* **54**, 11169 (1996).
49. Perdew, J. P., Burke, K. & Ernzerhof, M. Generalized gradient approximation made simple. *Phys. Rev. Lett.* **77**, 3865 (1996).
50. Blöchl, P. E. Projector augmented-wave method. *Phys. Rev. B* **50**, 17953 (1994).
51. Monkhorst, H. J. & Pack, J. D. Special points for Brillouin-zone integrations. *Phys. Rev. B* **13**, 5188 (1976).
52. Momma, K. & Izumi, F. VESTA 3 for three-dimensional visualization of crystal, volumetric and morphology data. *J. Appl. Cryst* **44**, 1272–1276 (2011).

Acknowledgements

We gratefully acknowledge MEXT for a Grant-in-Aid for Scientific Research (JP15KT0062, JP26248006, JP20H02638, JP17H01057, JP17K06818, JP20K21171). This work was also financially supported by The Sumitomo Foundation and The Murata Science Foundation. The synchrotron radiation experiments were performed at BL23SU in SPring-8, with the approval of the Japan Synchrotron Radiation Research Institute (JASRI) and Japan Atomic Energy Agency (JAEA) (Proposal Nos. 2019B3801, 2019A3831, 2019A3801, 2018B3831, 2018B3801, 2018A3831, 2018A3801, 2017B3801, 2017A3801). This work was performed under the Shared Use Program of JAEA Facilities (Proposal Nos. 2019A-E13, 2018B-E12, 2018A-E17) with the approval of Nanotechnology Platform project supported by the Ministry of Education, Culture, Sports, Science and Technology. We are grateful for the assistance given by Naoyuki Shimode, Shizuka Nishi, Hikaru Yoshida and all the staffs at BL23SU in SPring-8. Structures and related figures appearing in the manuscript and in the Supplmentary information were drawn using the VESTA package[52].

Author contributions

M.O. conceived and directed the research. Y.T., T.M., A.Y. and M.O. performed all the experiments. Y.T. and M.O. carried out the data analyses. Y.T., J.S.G. and W.A.D. performed the theoretical calculations. All authors contributed to the manuscript preparation.

Competing interests

The authors declare no competing interests.

Additional information

Supplementary Information The online version contains supplementary material available at https://doi.org/10.1038/s41598-021-82180-w.

Correspondence and requests for materials should be addressed to Y.T., W.A.D. or M.O.

Reprints and permissions information is available at www.nature.com/reprints.

Publisher's note Springer Nature remains neutral with regard to jurisdictional claims in published maps and institutional affiliations.